Constructing Tunable Electrides on Monolayer Transition Metal Dichalcogenides

Yuanhui Sun,[1,2] Austin Ellis,[2] Saul Diaz,[2] Wei Li,[1,3] and Maosheng Miao,[2,]*

[1]Suzhou Laboratory, Suzhou, Jiangsu 215123, P. R. China

[2]Department of Chemistry and Biochemistry, California State University Northridge,
Northridge, CA 91330, United States

[3]Gusu Laboratory of Materials, Suzhou, Jiangsu 215123, P. R. China

Corresponding Author

*mmiao@csun.edu.

ABSTRACT

(150 words) Electrides have emerged as promising materials with exotic properties due to the presence of localized electrons detached from all atoms. Despite the continuous discovery of many new electrides, most of them are based on atypical compositions and their applications require an inert surface structure to passivate reactive excess electrons. Here, we demonstrated a different route to attain tunable electrides. We first report that monolayer transition metal dichalcogenides (TMDCs) exhibit weak electride characteristics, which is the remainder of electride feature of the transition metal sublattice. By introducing chalcogen vacancies, the enhanced electride characteristics are comparable to that of known electrides. Since the precise tailoring of chalcogen vacancy concentration has been achieved experimentally, we proposed that TMDCs can be used to build electrides with controllable intensities. Furthermore, we demonstrate that the electride states at chalcogen vacancy of monolayer TMDCs will play an important role in catalyzing hydrogen evolution reactions.

TOC GRAPHICS

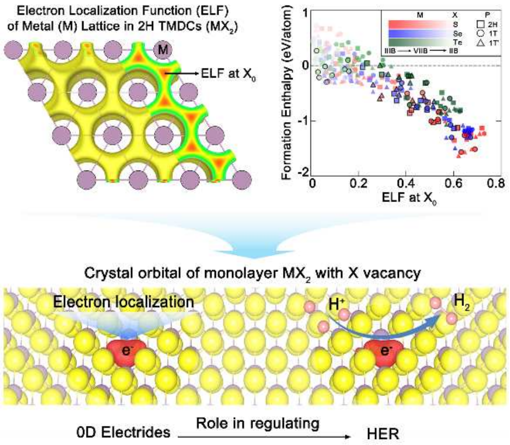

KEYWORDS: Electrides, Transition metal dichalcogenides, Hydrogen evolution reaction, Density functional calculation

Materials that contain electrons in the void or interlayer space exhibiting the role of anions are called electrides.[1,2] One beneficial property of electrides is that their interstitial anionic electrons can be easily transferred or emitted into a surface reactant or vacuum when they are exposed to reactive atmospheres or activated by an electric field, triggering chemical reactions and actuating electronic devices.[3–5] Most synthesized organic electrides were highly sensitive to heat and oxidation,[6–9] which hinders the investigation of possible applications and has stimulated the enthusiasm of the identification on chemically stable electrides under ambient conditions. Ambient-stable electrides are rare and always require an inert surface structure to passivate the reactive excess electrons. Most of the electrides present atypical compositions and assume complex structures. In 2003, the synthesis of first inorganic electride $[Ca_{24}Al_{28}O_{64}]^{4+}\cdot 4e^{-}$ (C12A7:e^{-}) with enhanced thermal and chemical stability was reported.[10] C12A7:e^{-} exhibits a low work function of 2.4 eV at room temperature, which facilitates various practical applications in electronics and catalysis.[2,3,10–12] However, electrons near its surface readily react with water and oxygen, forming an electron deficient layer during the synthesis process.[12,13] To realize the activity of interstitial anionic electrons in electrides, additional polishing or sputter etching is applied to remove the inert layer.[10,14]

In 2013, the synthesis of first two-dimensional (2D) layered electride Ca_2N ($Ca_2N:e^{-}$) was reported, in which the anionic electrons are confined in the interlayer place of two neighboring $[Ca_2N]^{+}$ slabs and are depicted as 2D electron gas (2DEG).[15] $Ca_2N:e^{-}$ provides an superior electron mobility (~200 cm^{2} V^{-1} s^{-1}) than that of C12A7:e^{-} (~4 cm^{2} V^{-1} s^{-1}).[10,15] However, the exposed excess electrons are chemically active at ambient conditions,[16] and an effective encapsulation is needed for electronic applications. Liquid-phase exfoliation offers additional advantages to exfoliate $Ca_2N:e^-$ into 2D electride flakes, called electrene[17] following the naming rule in 2D materials such as graphene, while its surface is also oxidized during the exfoliation process or subsequent handling.[18] The self-passivated reaction can help to turn dihafnium sulfide into a chemically stable 2D layered electride in strongly oxidative water and acid solutions, which has been demonstrated to have persistent electrocatalytic characteristics.[19] Moreover, other stable electrides have been found in intermetallic compounds, such as Y_5Si_3 and LaScSi, but their surface structures need to be investigated.[20,21] First-principles density functional theory (DFT) calculations were also actively carried out screening new electrides with variant properties and superior functions, the most widely accepted rule is the compound must be electron-rich.[22–27] To our knowledge, however, electrochemical catalysts composed of electrides capable of reacting directly on their surfaces have not been reported so far.

In this work, we propose and demonstrate a new route of study that can attain controllable electride states on stable 2D materials, namely the monolayer TMDCs. Monolayer TMDCs are one of the most popular 2D materials beyond graphene,[28] which can be easily obtained by mechanical peel-off,[29,30] liquid-phase exfoliation,[31,32] epitaxial growth,[33,34] chemical vapor deposition,[35,36] and etc. from their layered compounds. Their structure stability was also confirmed by the applications under different conditions, for example, enormous electrocatalysts and photocatalysts in electrolyte with different pH values,[37–41] strain engineering for applications in optics and electronics,[42–44] and high-frequency operation in transistor devices.[45–47] These physical or chemical processes are all happened directly on the surface or the edges of 2D TMDCs, rather than the contaminated surface layer.

Based on first-principles DFT calculations, we show that the electride nature of the transition metal (TM) sublattices in TMDCs is a determining factor that stabilizes the compound, and some remainder localization features are found in the interstitial sites between 3 metal atoms and 6 chalcogen atoms of monolayer TMDCs, showing weak electride characteristics. More significantly, our calculations show that the chalcogen vacancies create considerable amount of localized electrons, reaching the same values as other reported electrides.[3,20] Chalcogen vacancies are the most common defects in TMDCs, and recent experiments showed the creation of them with controllable density and excellent stability.[48–52] For example, the sulfur vacancies can be produced to an optimum density of 4.7% in monolayer 2H-MoS_2 to realize a record high carrier mobility (> 115 cm^2 V^{-1} s^{-1}).[53] Therefore, our work might provide a route to attain electrides with controllable concentrations of anionic electrons, which is a distinct advantage over many commonly known electrides such as Ca_2N:e^- and its nanosheets.[15,18,54] Furthermore, we demonstrated that such attained electride will play an important role in controlling the hydrogen evolution reaction (HER) performance of monolayer TMDCs.

The underlying first-principles DFT calculations were carried out by using the plane-wave pseudopotential method as implemented in Vienna Ab initio Simulation Package (VASP).[55,56] The electron-ion interactions were described by the projector augmented wave pseudopotentials.[57,58] We used the generalized gradient approximation formulated by Perdew, Burke, and Ernzerhof as exchange-correlation functional.[59] A kinetic energy cutoff of 600 eV was adopted for wave-function expansion. The electronic integration within the Brillouin zone was done with the k-point meshes of 15×15×1 and 2×2×1 for the monolayer primitive cell and the corresponding 7×7×1 supercell, respectively. A vacuum layer more than 20 Å was used in the calculations to isolate the monolayer from its neighboring image. Structures were fully optimized including van der Waals (vdW) interaction,[60,61] until the residual force were converged within 0.02 eV $Å^{-1}$. The electronic localization of structures are evaluated using the ELF.[62] The high-throughput first-principles DFT calculations were performed by using the Jilin Artificial-intelligence aided Materials-design Integrated Package (JAMIP), which is an open-source artificial-intelligence-aided data-driven infrastructure designed purposely for computational materials informatics.[63]

For a given monolayer 2H-MX_2 with chalcogen vacancy, two electron charge densities are calculated, including a self-consistent charge density with net charge ($CHGCAR_{nc}$) and a self-consistent charge density with adding 0.2 e^- charge ($CHGCAR_{nc+0.2}$) or removing 0.2 e^- charge ($CHGCAR_{nc-0.2}$). The charge density difference is then calculated as $\Delta CHGCAR = CHGCAR_{nc\pm0.2} - CHGCAR_{nc}$. The $\Delta CHGCAR = 0$ surface divides the structure into electron-gaining and electron-losing parts, which are colored yellow and cyan, respectively.

Calculations on HER free energies were performed at the chalcogen vacancy sites of monolayer 2H-MX_2 in a 7×7×1 supercell. For all the studied structures, the free energies were evaluated by the following expression

$$\Delta G(H^*) = \Delta E(H^*) + \Delta E_{ZPE} - T\Delta S \qquad (1)$$

where $\Delta E(H^*)$, ΔE_{ZPE}, and ΔS are the binding energy, zero-point energy change and entropy change of H^* adsorption, respectively. T is the temperature (300 K) and * means the active sites at chalcogen vacancy defects. The binding energy $\Delta E(H^*)$ of H atoms at * was calculated by the following equation

$$\Delta E(H^*) = E(surf+H^*) - E(surf) - \tfrac{1}{2} E(H_2) \quad (2)$$

where $E(surf+H^*)$ and $E(surf)$ are the total energies with and without H absorption, respectively. In this work, the $T\Delta S$ and ΔE_{ZPE} are obtained by following the scheme proposed by Norskov et al.[64] Specifically, ΔS can be got using equation $\Delta S = S(H^*) - 1/2\ S(H_2) \approx -1/2\ S(H_2)$, in view of the negligible vibrational entropy of H^*. Thus, we can easily conclude that $T\Delta S$ is −0.205 eV, since $TS(H_2)$ is known to be 0.41 eV at 300 K and 1 atmosphere. ΔE_{ZPE} for H^* is estimated by equation $\Delta E_{ZPE} = E_{ZPE}(H^*) - 1/2\ E_{ZPE}(H_2)$. Our calculated $E_{ZPE}(H_2)$ is about 0.306 eV, which is close to the one reported by Norskov et al.[64] The detailed results are listed in Table S1.

Electride features of the TM sublattices and the stability of TMDCs. TMDCs are among the most popular 2D layered materials beyond graphene,[28] which are semiconductors of type MX_2, where M is a transition metal atom (such as Mo or W) and X is a chalcogen atom (S, Se, or Te). Bulk TMDCs crystals are stacked by individual MX_2 layers (in atomic sequence of [X–M–X]), in which three common monolayer polymorphs are characterized by either trigonal prismatic (2H) or octahedral (1T), distorted 1T' coordination of M atoms.[28] It is worth mentioning that their M atoms form either a perfect close-packed hexagonal monolayer or a distorted one (Figures 1a-c).

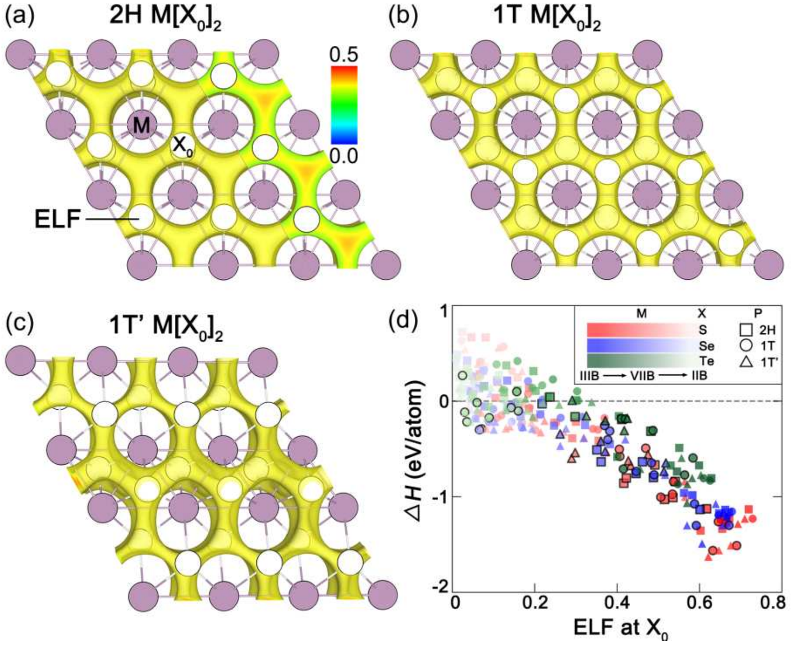

Figure 1. Stability of monolayer TMDCs. (a-c) Schematic ELF distributions of M layer in monolayer 2H, 1T, 1T' MX_2. The M atoms are colored light purple, and the positions of X atoms in MX_2 (depicted as X_0) are added as white balls to show the relative locations with respect to the ELF maxima of M layer. We take M = Mo and X = S as an example to plot Figs. 1a-c. A slab cut on upper S layer of ELF is illustrated in Figure 1a. (d) Evolution of stability of monolayer MX_2 as a function of ELF at X_0 position. All 30 transition metals are considered, and the color of M gradually becomes lighter from early transition metals to later transition metals. The synthesized monolayer TMDCs are marked with black frames.

Our calculations reveal a striking correlation between the electron localization of TM sublattices and the stability of the TMDCs. Our recent studies have shown electron localizations in the interstitial orbitals (quasi-atoms) of many 3D lattices of early transition metals and their critical roles in determining the complex structure change pattern of elemental metals[65] as well as the formation of stable superhydrides.[66] These results encourage us to study the electron localizations in the TM sublattices in a monolayer TMDC, e.g. the Mo 2D hexagonal sublattice after removing S atoms in monolayer MoS_2. We first calculated electron localization function (ELF) of Mo sublattices in three polymorphs of MoS_2. They all show patterns of maxima above or below the Mo plane and at the center among three Mo atoms. Half of these sites are where the S atoms were originally located (Figures 1a-c). To show the electron localization shapes more clearly, the 2D slices along the S plane of 2H-MS_2 with M in VB and VIB groups are shown in Figure S1. The electron localization at these off-plane interstitial sites in the Mo sublattice has also been confirmed by the density difference, i.e., the difference between the electron density of the Mo lattice and that of Mo atoms.

To demonstrate the generalizability of the study, all 30 transition metals are considered to form 2H, 1T, and 1T' polymorphs of monolayer MX_2 (X = S, Se, or Te), no matter it has been synthesized or not. The formation enthalpies are measured by $\Delta H = (H(MX_2) - H(M) - 2H(X))/3$, where $H(MX_2)$ is the enthalpy of monolayer MX_2, H(M) and H(X) are the enthalpies of the most stable structures of M and X elements, respectively. Our results show that the ΔH of monolayer TMDCs are strongly correlated to the ELF values at the maxima (Figure 1d), which strongly suggest that the structure stabilities will be enhanced whence the corresponding M lattices can generate larger electron densities and localizations at interstitial positions. This observation is true for both synthesized (marked with black frames) and hypothetical monolayer TMDCs, and may also be generalized to other 2D materials.

Similar to metal superhydrides, the localized electrons of the TM sublattice at the sites of S atoms naturally fill their 3p orbitals. On the other hand, the localized electrons at the off-plane interstitial sites without S atoms need to transfer to occupy S 3p orbitals, which will suppress the electride feature of the TM sublattice. In many 3D compounds such as KCl, the similar electron transference is complete, causing the electride features in metal lattices to diminish. Surprisingly, our calculations show many 2H-MX_2 (M = Mo or W; X = S or Se) are weak electrides because there are remaining anionic electrons occupying their interstitial sites. We will take monolayer 2H-MoS_2 as an example to discuss the electronic properties of this weak electride.

Electronic property analysis of 2H TMDCs electrides. The ELF of 2H-MoS_2 shows maxima (depicted as E in Figure 2a) at the center of the voids surrounded by 3 Mo atoms and 6 S atoms. However, ELF alone cannot determine whether a compound is an electride. We, therefore, calculated the charge density difference between 2H-MoS_2 and the corresponding Mo/S atoms. As shown in Figure 2b, it also exhibits local maxima at the same sites of the ELF maxima (lower panel of Figure 2a), confirming that electrons are localized at the interstitial sites and occupy the corresponding "quasi-atom" orbitals.[67,68] To identify the contribution of interstitial anionic electrons, the projected band structure, or fat bands, and projected density of states (PDOS) of monolayer 2H-MoS_2 are plotted in Figure 2c. We placed empty spheres, representing the quasi-atoms.[67,68] with a Wigner-Seitz radius of 0.6 Å at the E centers. Both fat bands and PDOS show that the quasi-atoms orbitals contribute mainly to the electron states connecting M and K points in the energy range from 0 to 1 eV below the Fermi level. Thus, the electronic structure characteristics of 2H-MoS_2 clearly classify it as an electride. This electride behavior is also observed in various other TMDCs, such as 2H-$MoSe_2$, 2H-WS_2, and 2H-WSe_2. However, such features are entirely absent in other TMDC polymorphs like 1T- and 1T'-MX_2. Apart from TMDCs, $LaBr_2$ is the only monolayer compound exhibiting similar electride properties, though it remains almost unexplored.[25,69]

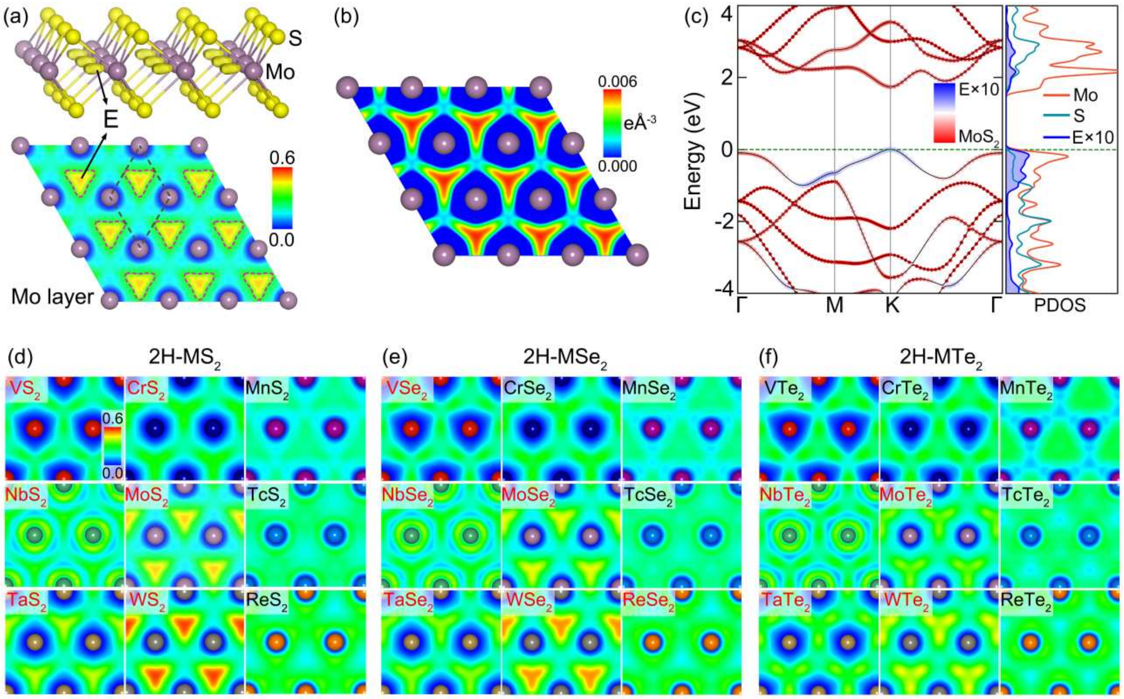

Figure 2. Crystal structure and the electronic structure of monolayer 2H TMDCs electride. (a) crystal structure of monolayer 2H-MoS_2 (upper panel) and corresponding slab cut on Mo layer of the ELF (lower panel). The Mo and S atoms are colored light purple and yellow, respectively. The interstitial anionic electrons (E) are marked with magenta dashed frames. (b) The slab cut on Mo layer of the charge density difference between 2H-MoS_2 and corresponding Mo/S atoms. (c) The projected band structure and PDOS of monolayer 2H-MoS_2. The value of E has been enlarged by a factor of ten to show the results more clearly. (d-f) Slab cuts on M layer of the ELF of monolayer 2H-MX_2, where M is a transition metal of Group 5-7, X

is a chalcogen atom (S, Se, or Te). The synthesized monolayer 2H-MX_2 are marked with red chemical formula.

The strength of the electride features in TMDCs strongly depends on the constituent metals, especially their positions in the periodic table. While the atomic number of metal increases, the values of ELF maxima at the voids (Figure S2) increase and maximize at group 6 metals (Cr, Mo, and W). This trend aligns closely with the variation in electride strength within the metal sublattice. This is a direct consequence of the electride properties of TMDCs being remnants of the localized electrons in metals. Consequently, the stability of 2H-MX_2 directly correlates with its electride strength. As a matter of fact, all the 2H-MX_2 with stronger electride features are the ones that have been successfully synthesized.

To show this trend more clearly, we plot the ELF of monolayer 2H-MX_2 on the metal plane for metals of Group 5-7 (Figures 2d-f). The chemical formulae of synthesized monolayer 2H-MX_2 are shown in red. They show that the synthesized TMDCs tend to possess larger electron localizations at the center of the void, especially for 2H-MoS_2, 2H-WS_2, 2H-$MoSe_2$, and 2H-WSe_2. Moreover, the intensity is enhanced when metal changes from Mo to W. The projected band structures and PDOSs of 2H-WS_2, 2H-$MoSe_2$, and 2H-WSe_2 show that their anionic electrons have comparable contributions as those of 2H-MoS_2 (Figure S3). Although the stability of MX2 and the ELF of the metal sublattices are strongly correlated, they do not follow a precise functional relationship. Furthermore, there is no definite relationship between the ELF, stability, and MX2 compounds synthesized in the lab. For example, monolayer 2H-VSe2

(ELF = 0.2) has been synthesized, while a hypothetical monolayer 2H-CrSe2 (ELF = 0.27) has not yet been synthesized. This can be attributed to several reasons: 1) Although ELF is a good indicator of electron localization, it cannot quantitatively describe the strength and density of localized electrons, nor can it be used to accurately compare compounds with different elements. 2) The thermodynamic stability of MX2 is not determined solely by its enthalpy of formation. It requires a thorough examination by calculating the full phase diagram or the binary convex hull of M-X compounds with different compositions. 3) The synthesis of MX2 compounds in the lab depends on many factors, both thermodynamic and kinetic, including the choice of reactants, the design of the reaction pathway, and the control of reaction conditions. It is not unusual for a metastable compound above the convex hull to be synthesized in the lab. It is also important to notice that the electride features in monolayer 2H-MoS_2, 2H-WS_2, 2H-$MoSe_2$, and 2H-WSe_2 are rather weak and might not be directly used in catalysis and electronic devices.

Enhancing electride strength in monolayer 2H TMDCs by chalcogen vacancies. Our calculations show that introducing defects, especially chalcogen vacancies, can greatly enhance the electride feature of 2H TMDCs. The most common defects in TMDCs are vacancies and the anti-sites.[52,71,72] A wide variety of intrinsic defects has been found in monolayer MoS_2.[48–50] including a single S vacancy (V_S), double S vacancy (V_{S2} or V'_{S2}), Mo atom occupies one S atom (Mo_S), Mo atom occupies two S atoms (Mo_{S2}), a single Mo vacancy (V_{Mo}), etc. We simulated the V_S, V_{S2}, V'_{S2}, Mo_S, Mo_{S2}, and V_{Mo} defects on a 7×7×1 supercell model of monolayer MoS_2. The calculated ELF maps (Figure 3a) clearly show the isolated interstitial anionic electrons located at the sites of S vacancies in structures with V_S, V_{S2}, and V'_{S2} defects, but not in structures with Mo_S, Mo_{S2}, and V_{Mo} defects. The interstitial anionic electrons (also depicted as E here) are closer to Mo layer than S atoms in structures with V_S, V_{S2}, and V'_{S2} defects. Among these defects, V_S and V_{S2} are the two most common ones in monolayer 2H-MoS_2.[48] and the electron structure of a V'_{S2} is comparable to the overlap of two adjacent V_S. We, therefore, will focus on structures with V_S or V_{S2} defect in the following discussion.

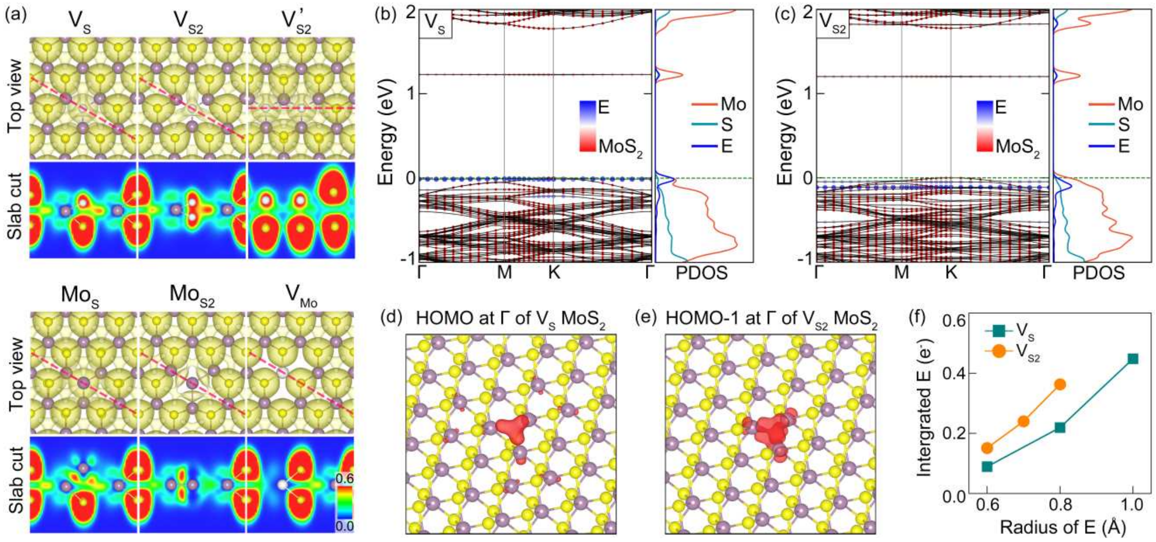

Figure 3. Electronic structures of monolayer 2H-MoS_2 with defects in a 7×7×1 supercell. (a) From left to right from top to bottom: ELF maps of monolayer 2H-MoS_2 with V_S, V_{S2}, V'_{S2}, Mo_S, Mo_{S2}, or V_{Mo} defect in a 7×7×1 supercell, respectively. The slab cuts show the ELF distribution along the magenta dashed line marked in top view of the structure. To show the results clearly, we added a white ball at the site of S or Mo vacancy in ELF maps. (b-c) The projected band structure and PDOSs of monolayer V_S 2H-MoS_2 and V_{S2} 2H-MoS_2 electrides, respectively. Partial charge densities (red) of (d) HOMO at Γ point of monolayer V_S 2H-MoS_2 and (e) HOMO−1 at Γ point of monolayer V_{S2} 2H-MoS_2, respectively. (f) Evolution of the integrated electrons of each E as a function of chosen Wigner-Seitz radius. The distance between E and nearest neighbor Mo atoms in monolayer V_S 2H-MoS_2 is about 2.0 Å, hence its maximum Wigner-Seitz radius of E is set to 1.0 Å. And

the distance between two Es in monolayer V_{S2} 2H-MoS_2 is about 1.6 Å, hence its maximum Wigner-Seitz radius of E is set to 0.8 Å.

The projected band structures and PDOSs of monolayer 2H-MoS_2 with V_S or V_{S2} defect in a 7×7×1 supercell are plotted in Figures 3b-c. To make a comparison with that in pristine monolayer 2H TMDCs, the quasi-atom (E) is also set to a Wigner-Seitz radius of 0.6 Å here. For 2H-MoS_2 with V_S defect (V_S 2H-MoS_2), the contribution from E is mainly distributed at the highest valence band. The calculated PDOS shows that the contribution of E to electronic properties is comparable to Mo atoms (Figure 3b). Similarly, the top of valence bands in 2H-MoS_2 with V_{S2} defect (V_{S2} 2H-MoS_2) also exhibit large contributions from E (Figure 3c). The importance of the quasi-atom states is also visible in the partial charge densities of the highest occupied molecular orbital (HOMO) at Γ point of V_S 2H-MoS_2 (Figure 3d) and HOMO−1 at Γ point of V_{S2} 2H-MoS_2 (Figure 3e), respectively. Meanwhile, we also compared the influences of different defect density on the electronic properties. The results show that the outcomes in the 5×5×1 supercell are almost identical to those in the 7×7×1 supercell (Figure S4). This result also demonstrates that the electride characteristics in defected MoS2 are determined by localized electrons, which do not interact when positioned far apart.

Similar electron localization has been observed before, but its relation to electride has not been noticed.[73,74] The quasi-atom states also contribute considerably to the lowest conduction band(s). Because the electron states in conduction bands are more delocalized, the Wigner-Seitz radius of 0.6 Å is too small to include major contributions from quasi-atoms. While calculating PDOS as a function of E radius (Figures 3f and S5), we found that the contribution of E occupancy increases with increasing radius. The integrated electrons of E in PDOS reach 0.45 e^- and 0.36 e^- for monolayer V_S 2H-MoS_2 (Wigner-Seitz radius of 1.0 Å) and V_{S2} 2H-MoS_2 (Wigner-Seitz radius of 0.8 Å) defects, respectively.

Moreover, we extended the V_S and V_{S2} defects into other monolayer MX_2 (M is a transition metal in Group Ⅴ–Ⅶ). For structures with single X vacancy (V_X) defect, MoX_2 and WX_2 (X = S, Se, or Te) show obvious E at the site of V_X defect (Figure S6). While for structures with double X vacancy (V_{X2}) defect, almost all investigated structures show obvious E at the site of V_{X2} defect, in which the synthesized structures show stronger distribution as indicated by ELF maps (Figure S7). In addition, the intensity of interstitial anionic electrons increases when metals change from 4th to 5th, and to 6th row in the periodic table of elements. The projected band structures and PDOSs of representative monolayer 2H-MX_2 (M = Mo, W; X = S, Se, or Te) with V_S and V_{S2} defect in a 7×7×1 supercell are plotted in Figures S8 and S9, respectively. It is worth mentioning that the intensity of E in them is comparable to that in 2H-MoS_2, but only the energy level of E in 2H-MoS_2 with V_S or V_{S2} defect mainly occupies the VBM, the quasi-atom states in other structures occupy the deeper valence bands.

Despite the variations of E states in different TMDCs, all electron structure analyses show evidence that monolayer 2H-MX_2 (especially for M = Mo, W, and X = S, Se, or Te) with chalcogen vacancies are new 0D electrides embedded on well-studied 2D materials. Due to the ubiquity of chalcogen vacancies, it has become an important approach to tune the optical and electronic properties of monolayer or few-layer TMDCs.[71,72] In particular, by purposely tailoring the V_S to an optimum density of 4.7% in monolayer 2H-MoS_2, a record-high carrier mobility (>115 cm^2 V^{-1} s^{-1}) is achieved.[53] This means that we have been able to precisely control the strength of electride characteristics in 2H-MoS_2 or other TMDCs, which is more flexible than the layer distributed 2DEG in $Ca_2N:e^-$ and its nanosheets.[15,18,54]

Catalytic effects of monolayer TMDC electrides on HER. The significant catalytic effects of V_X in 2D TMDC on HER have attracted intensive studies.[41,51,75–77] We will study the role of the electrides and demonstrate that the electride nature of the defected TMDC can be utilized to control and enhance the catalytic efficiency. In our study, the hydrogen absorption free energies (ΔG) of monolayer 2H-MX_2 (M = Mo, W; X = S, Se, or Te) with V_X defect are calculated in a 7×7×1 supercell. The obtained ΔG is in the range of –0.2 to 0.25 eV/H, which is close to that in previous calculations.[41,51] Because the defected 2H-MX_2 are electrides, their catalytic activities might be influenced by the amount of localized electrons, which can be controlled by charge transfer through doping or applying an electric field. We simulate such a process by adding or extracting electrons in the supercell models. A similar electron traversing effect has been proven by encapsulating a precisely grown double-layer MoS_2/graphene heterostructure and a CoNi nanoalloy.[78] It tunes the electronic structures of V_S defect in basal plane, resulting in more appropriate ΔG on the active positions.

Besides HER catalyst TMDCs, we also include the V_S defect in monolayer 2H-NbS_2 using the 7×7×1 supercell. Nb element is next to Mo in the periodic table, and defected 2H-NbS_2 is not an electride and does not show good HER performance.[73] As shown in Figure 4a, the ΔG of 6 monolayer 2H-MX_2 decreases significantly no matter adding or removing electrons to the structure. Among them, 2H-MoS_2, 2H-WS_2, and 2H-WSe_2 with V_S defect reach the optimal ΔG=0 eV at a condition of removing 0.07, 0.21, and 0.15 e^-, respectively. While the slopes are flatter at the part of adding electrons, leading to more electrons are required to reach the optimal ΔG=0 eV. In contrast, the evolution of ΔG with varying numbers of electrons in monolayer V_S 2H-NbS_2 is almost a horizontal line, which is different from those in V_X 2H-MX_2. A hereafter question is why electron transfer affects the HER catalytic activity in monolayer V_X 2H-MX_2 (M=Mo, W) but not in monolayer V_S 2H-NbS_2.

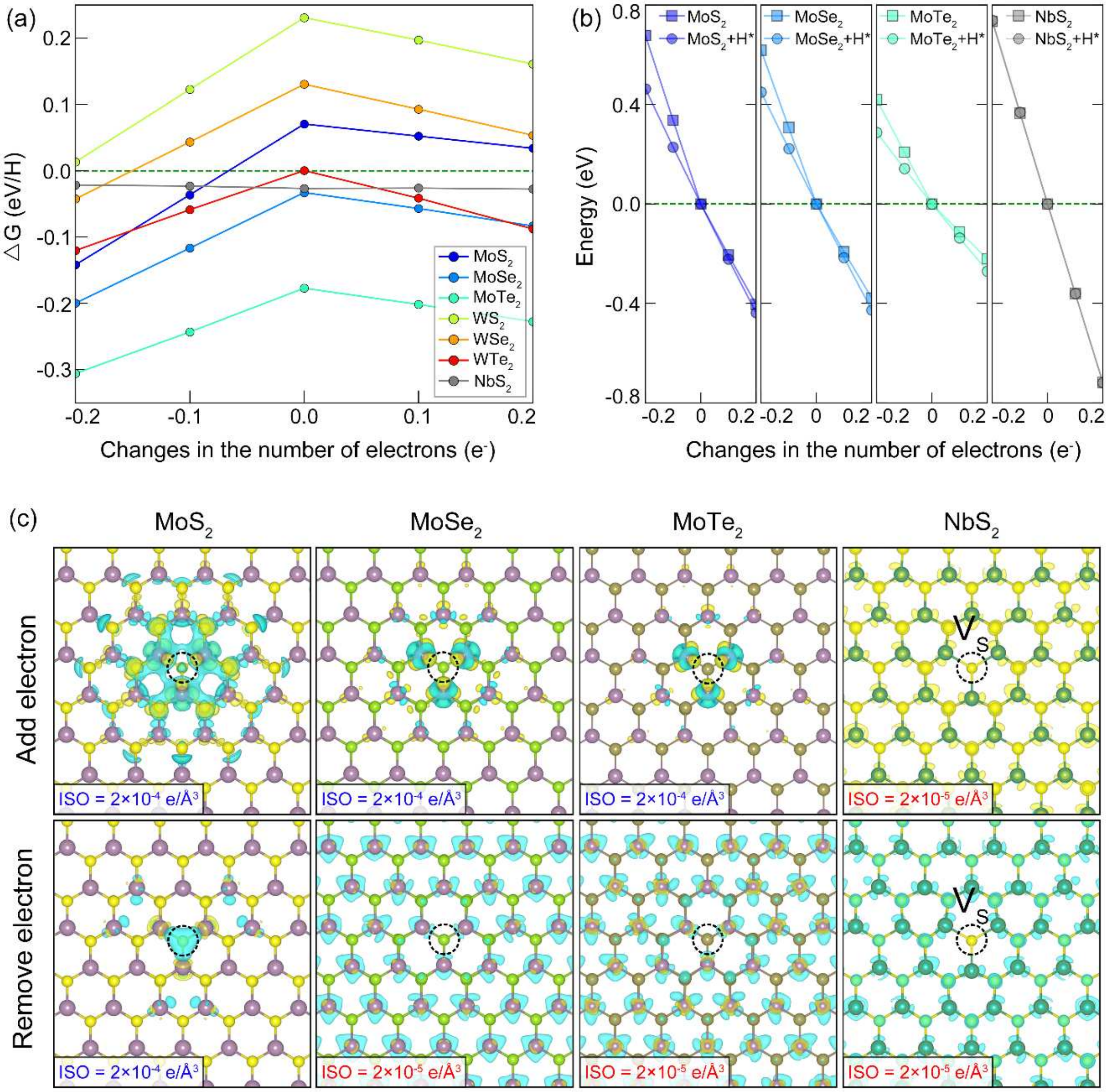

Figure 4. Effects of monolayer V_X 2H-MX_2 electrides on HER activity. (a) Evolutions of ΔG as a function of changes in the number of electrons, ranging from removing 0.2 e^- to adding 0.2 e^- in a 7×7×1 supercell. (b) Evolutions of E(surf+H*) and E(surf) as a function of changes in the number of electrons, ranging from removing 0.2 e^- to adding 0.2 e^-. The E(surf+H*) and E(surf) with new charges are set to zero. (c) The charge density difference of V_X 2H-MX_2 before and after adding (upper panel) or removing (lower panel) 0.2 e^-. The isosurface values (ISO) are set to 2×10^{-4} e/Å^3 or 5×10^{-5} e/Å^3 according to the degree of electron

distribution. To clearly illustrate the site of vacancy defects, the V_S sites are marked with dashed black circles.

According to Table S1 and computational methods, the evolution of ΔG is mainly dominated by the energy difference between E(surf+H*) and E(surf). The evolutions of E(surf+H*) and E(surf) with adding/removing electrons in the structure are shown in Figures 4b and S10b. The energies of these structures with net charges are set to zero for easy comparison. We can see that the evolutions of E(surf+H*) and E(surf) of V_S 2H-NbS_2 are almost coincident with varying number of electrons, while the curves are separated in V_X 2H-MX_2 (M = Mo, W; X = S, Se, or Te). The evolutions of their E(surf+H*) are almost linear, but the slopes of the E(surf) curves of each structure are different when adding or removing electrons, implying that they are controlled by different mechanisms. Therefore, we analyzed the charge density difference before and after adding/removing electrons to the structure (see computational methods). As shown in Figures 4c and S10c, when 0.2 e^- is added to V_X 2H-MoX_2 or V_X 2H-WX_2 (upper panel), the electron distribution around 3 nearest neighboring Mo/W atoms to V_X defect changes drastically, and the intensity decreases as X goes from S→Se→Te. On the other hand, when 0.2 e^- is removed from V_X 2H-MoX_2 or V_X 2H-WX_2 (lower panel), only the electron source in V_S 2H-MoS_2 comes from its V_S defect, while it is the contribution from all Mo/W atoms in other structures. These results are implied in their projected band structures and PDOSs as shown in Figure S8. When VX defect exists in MoX_2 or WX_2, it will bring a new lowest conduction band, which is contributed by the empty d orbitals of 3 nearest neighboring

Mo/W atoms to V_X defect. The added electrons mostly occupy this energy band. Moreover, when removing the number of electrons in the structure, VBM will lose electrons first. Only the VBM of V_S 2H-MoS_2 is occupied by the electrons of V_S defect, but it mainly comes from all Mo/W atoms in other structures. However, the situation in V_S 2H-NbS_2 is totally different, all its Nb and S atoms will participate in whether adding or removing electrons to the structure, but no V_S-related contributions are found, which can also be seen from its projected band structure and PDOSs (Figure S11). This helps to explain why its E(surf) is linearly related to the change of number of electrons in the structure. The mechanism relies on the fact that the quasi-atom state at V_X site plays an important role in regulating the HER process of monolayer 2H TMDCs.

In conclusion, our comprehensive DFT calculations and electronic structure analyses reveal an unexpected finding: many 2D TMDCs, including MoS_2, are inherently weak electrides. Their electride potency can be significantly amplified by introducing chalcogen vacancies. The corresponding localized electrons play a pivotal role in defining the material's properties. The HER catalytic activities of TMDCs with defects are largely driven by their electride nature. This can be further optimized by modulating electron transfer via doping or the application of an electric field. Given that the concentration of V_S defects can be precisely controlled in monolayer MoS_2, our research illuminates a novel pathway to craft electrides from a family of extensively studied monolayer materials, offering both adjustable intensity and functionality. Our work thus bridges two previously separate areas of materials science: 2D (or monolayer) materials and electrides.

ASSOCIATED CONTENT

Supporting Information. The supporting Information is available free of charge at XXX.

Electronic properties of monolayer 2H-MX_2, Electronic properties of monolayer 2H-MX_2 with chalcogen vacancy defects, Hydrogen evolution reaction performance of monolayer 2H-MX_2 with single chalcogen vacancy, Electronic properties of monolayer 2H-NbS_2 with single S vacancy, The calculation of free energies. (PDF)

AUTHOR INFORMATION

Notes

The authors declare no competing financial interests.

ACKNOWLEDGMENT

M.M. and Y.S. acknowledge the support of NSF under grant Nos. DMR 1848141 and OAC-2117956, as well as the support of the Department of Defense under grant No. W911NF2310232. M.M., A. E., and S. D. also acknowledge the support of the Camille and Henry Dreyfus Foundation and the California State University RSCA awards. W.L. was supported by Jiangsu Province Innovation Support Program (Soft Science Research) under grant No. BK20231215.

REFERENCES

(1) Dye, J. L. Electrides: Early Examples of Quantum Confinement. *Acc. Chem. Res.* **2009**, *42*, 1564–1572.

(2) Hosono, H.; Kitano, M. Advances in Materials and Applications of Inorganic Electrides. *Chem. Rev.* **2021**, *121*, 3121–3185.

(3) Kitano, M.; Inoue, Y.; Yamazaki, Y.; Hayashi, F.; Kanbara, S.; Matsuishi, S.; Yokoyama, T.; Kim, S.-W.; Hara, M.; Hosono, H. Ammonia Synthesis Using a Stable Electride as an Electron Donor and Reversible Hydrogen Store. *Nat. Chem.* **2012**, *4*, 934–940.

(4) Buchammagari, H.; Toda, Y.; Hirano, M.; Hosono, H.; Takeuchi, D.; Osakada, K. Room Temperature-Stable Electride as a Synthetic Organic Reagent: Application to Pinacol Coupling Reaction in Aqueous Media. *Org. Lett.* **2007**, *9*, 4287–4289.

(5) Toda, Y.; Matsuishi, S.; Hayashi, K.; Ueda, K.; Kamiya, T.; Hirano, M.; Hosono, H. Field Emission of Electron Anions Clathrated in Subnanometer-Sized Cages in $[Ca_{24}Al_{28}O_{64}]^{4+}(4e^{-})$. *Adv. Mater.* **2004**, *16*, 685–689.

(6) Le, L. D.; Issa, D.; Van Eck, B.; Dye, J. L. Preparation of Alkalide and Electride Films by Direct Vapor Deposition. *J. Phys. Chem.* **1982**, *86*, 7–9.

(7) Ellaboudy, A.; Dye, J. L.; Smith, P. B. Cesium 18-Crown-6 Compounds. A Crystalline Ceside and a Crystalline Electride. *J. Am. Chem. Soc.* **1983**, *105*, 6490–6491.

(8) Dawes, S. B.; Ward, D. L.; Huang, R. He.; Dye, J. L. First Electride Crystal Structure. *J. Am. Chem. Soc.* **1986**, *108*, 3534–3535.

(9) Singh, D. J.; Krakauer, H.; Haas, C.; Pickett, W. E. Theoretical Determination That Electrons Act as Anions in the Electride $Cs^{+}(15\text{-Crown-5})_2\cdot e^{-}$. *Nature* **1993**, *365*, 39–42.

(10) Matsuishi, S.; Toda, Y.; Miyakawa, M.; Hayashi, K.; Kamiya, T.; Hirano, M.; Tanaka, I.; Hosono, H. High-Density Electron Anions in a Nanoporous Single Crystal: $[Ca_{24}Al_{28}O_{64}]^{4+}(4e^{-})$. *Science* **2003**, *301*, 626–629.

(11) Hosono, H.; Kim, J.; Toda, Y.; Kamiya, T.; Watanabe, S. Transparent Amorphous Oxide Semiconductors for Organic Electronics: Application to Inverted OLEDs. *Proc. Natl. Acad. Sci.* **2017**, *114*, 233–238.

(12) Toda, Y.; Yanagi, H.; Ikenaga, E.; Kim, J. J.; Kobata, M.; Ueda, S.; Kamiya, T.; Hirano, M.; Kobayashi, K.; Hosono, H. Work Function of a Room-Temperature, Stable Electride $[Ca_{24}Al_{28}O_{64}]^{4+}(e^{-})_4$. *Adv. Mater.* **2007**, *19*, 3564–3569.

(13) Kim, S. W.; Hosono, H. Synthesis and Properties of $12CaO{\cdot}7Al_2O_3$ Electride: Review of Single Crystal and Thin Film Growth. *Philos. Mag.* **2012**, *92*, 2596–2628.

(14) Toda, Y.; Kubota, Y.; Hirano, M.; Hirayama, H.; Hosono, H. Surface of Room-Temperature-Stable Electride $[Ca_{24}Al_{28}O_{64}]^{4+}(e^{-})_4$: Preparation and Its Characterization by Atomic-Resolution Scanning Tunneling Microscopy. *ACS Nano* **2011**, *5*, 1907–1914.

(15) Lee, K.; Kim, S. W.; Toda, Y.; Matsuishi, S.; Hosono, H. Dicalcium Nitride as a Two-Dimensional Electride with an Anionic Electron Layer. *Nature* **2013**, *494*, 336–340.

(16) Zhao, S.; Li, Z.; Yang, J. Obtaining Two-Dimensional Electron Gas in Free Space without Resorting to Electron Doping: An Electride Based Design. *J. Am. Chem. Soc.* **2014**, *136*, 13313–13318.

(17) Druffel, D. L.; Woomer, A. H.; Kuntz, K. L.; Pawlik, J. T.; Warren, S. C. Electrons on the Surface of 2D Materials: From Layered Electrides to 2D Electrenes. *J. Mater. Chem. C* **2017**, *5*, 11196–11213.

(18) Druffel, D. L.; Kuntz, K. L.; Woomer, A. H.; Alcorn, F. M.; Hu, J.; Donley, C. L.; Warren, S. C. Experimental Demonstration of an Electride as a 2D Material. *J. Am. Chem. Soc.* **2016**, *138*, 16089–16094.

(19) Kang, S. H.; Bang, J.; Chung, K.; Nandadasa, C. N.; Han, G.; Lee, S.; Lee, K. H.; Lee, K.; Ma, Y.; Oh, S. H.; Kim, S.-G.; Kim, Y.-M.; Kim, S. W. Water- and Acid-Stable Self-Passivated Dihafnium Sulfide Electride and Its Persistent Electrocatalytic Reaction. *Sci. Adv.* **2020**, *6*, eaba7416.

(20) Lu, Y.; Li, J.; Tada, T.; Toda, Y.; Ueda, S.; Yokoyama, T.; Kitano, M.; Hosono, H. Water Durable Electride Y_5Si_3: Electronic Structure and Catalytic Activity for Ammonia Synthesis. *J. Am. Chem. Soc.* **2016**, *138*, 3970–3973.

(21) Wu, J.; Gong, Y.; Inoshita, T.; Fredrickson, D. C.; Wang, J.; Lu, Y.; Kitano, M.; Hosono, H. Tiered Electron Anions in Multiple Voids of LaScSi and Their Applications to Ammonia Synthesis. *Adv. Mater.* **2017**, *29*, 1700924.

(22) Inoshita, T.; Jeong, S.; Hamada, N.; Hosono, H. Exploration for Two-Dimensional Electrides via Database Screening and Ab Initio Calculation. *Phys. Rev. X* **2014**, *4*, 031023.

(23) Zhang, Y.; Wang, H.; Wang, Y.; Zhang, L.; Ma, Y. Computer-Assisted Inverse Design of Inorganic Electrides. *Phys. Rev. X* **2017**, *7*, 011017.

(24) Zhu, Q.; Frolov, T.; Choudhary, K. Computational Discovery of Inorganic Electrides from an Automated Screening. *Matter* **2019**, *1*, 1293–1303.

(25) Zhou, J.; Shen, L.; Yang, M.; Cheng, H.; Kong, W.; Feng, Y. P. Discovery of Hidden Classes of Layered Electrides by Extensive High-Throughput Material Screening. *Chem. Mater.* **2019**, *31*, 1860–1868.

(26) Kang, S. H.; Thapa, D.; Regmi, B.; Ren, S.; Kim, Y.-M.; Kim, S.-G.; Kim, S. W. Chemically Stable Low-Dimensional Electrides in Transition Metal-Rich Monochalcogenides: Theoretical and Experimental Explorations. *J. Am. Chem. Soc.* **2022**, *144*, 4496–4506.

(27) Lee, S. Y.; Hwang, J.-Y.; Park, J.; Nandadasa, C. N.; Kim, Y.; Bang, J.; Lee, K.; Lee, K. H.; Zhang, Y.; Ma, Y.; Hosono, H.; Lee, Y. H.; Kim, S.-G.; Kim, S. W. Ferromagnetic Quasi-Atomic Electrons in Two-Dimensional Electride. *Nat. Commun.* **2020**, *11*, 1526.

(28) Manzeli, S.; Ovchinnikov, D.; Pasquier, D.; Yazyev, O. V.; Kis, A. 2D Transition Metal Dichalcogenides. *Nat. Rev. Mater.* **2017**, *2*, 17033.

(29) Radisavljevic B.; Radenovic A.; Brivio J.; Giacometti V.; Kis A. Single-layer MoS_2 transistors. *Nat. Nano.* **2011,** 6, 147–150.

(30) Novoselov, K. S.; Jiang, D.; Schedin, F.; Booth, T. J.; Khotkevich, V. V.; Morozov, S. V.; Geim, A. K. Two-Dimensional Atomic Crystals. *Proc. Natl. Acad. Sci. U. S. A.* **2005**, *102*, 10451–10453.

(31) Coleman, J. N.; Lotya, M.; O'Neill, A.; Bergin, S. D.; King, P. J.; Khan, U.; Young, K.; Gaucher, A.; De, S.; Smith, R. J.; Shvets, I. V.; Arora, S. K.; Stanton, G.; Kim, H.-Y.; Lee, K.; Kim, G. T.; Duesberg, G. S.; Hallam, T.; Boland, J. J.; Wang, J. J.; Donegan, J. F.;

Grunlan, J. C.; Moriarty, G.; Shmeliov, A.; Nicholls, R. J.; Perkins, J. M.; Grieveson, E. M.; Theuwissen, K.; McComb, D. W.; Nellist, P. D.; Nicolosi, V. Two-Dimensional Nanosheets Produced by Liquid Exfoliation of Layered Materials. *Science* **2011**, *331*, 568–571.

(32) Nicolosi, V.; Chhowalla, M.; Kanatzidis, M. G.; Strano, M. S.; Coleman, J. N. Liquid Exfoliation of Layered Materials. *Science* **2013**, *340*, 1226419.

(33) Joyce, B. A. Molecular Beam Epitaxy. *Rep. Prog. Phys.* **1985**, *48*, 1637.

(34) Dumcenco, D.; Ovchinnikov, D.; Marinov, K.; Lazić, P.; Gibertini, M.; Marzari, N.; Sanchez, O. L.; Kung, Y.-C.; Krasnozhon, D.; Chen, M.-W.; Bertolazzi, S.; Gillet, P.; Fontcuberta i Morral, A.; Radenovic, A.; Kis, A. Large-Area Epitaxial Monolayer MoS_2. *ACS Nano* **2015**, *9*, 4611–4620.

(35) Shi, Y.; Li, H.; Li, L.-J. Recent Advances in Controlled Synthesis of Two-Dimensional Transition Metal Dichalcogenides via Vapour Deposition Techniques. *Chem. Soc. Rev.* **2015**, *44*, 2744–2756.

(36) Zhan, Y.; Liu, Z.; Najmaei, S.; Ajayan, P. M.; Lou, J. Large-Area Vapor-Phase Growth and Characterization of MoS_2 Atomic Layers on a SiO2 Substrate. *Small* **2012**, *8*, 966–971.

(37) Asadi, M.; Kim, K.; Liu, C.; Addepalli, A. V.; Abbasi, P.; Yasaei, P.; Phillips, P.; Behranginia, A.; Cerrato, J. M.; Haasch, R.; Zapol, P.; Kumar, B.; Klie, R. F.; Abiade, J.; Curtiss, L. A.; Salehi-Khojin, A. Nanostructured Transition Metal Dichalcogenide Electrocatalysts for CO_2 Reduction in Ionic Liquid. *Science* **2016**, *353*, 467–470.

(38) Shi, J.; Tong, R.; Zhou, X.; Gong, Y.; Zhang, Z.; Ji, Q.; Zhang, Y.; Fang, Q.; Gu, L.; Wang, X.; Liu, Z.; Zhang, Y. Temperature-Mediated Selective Growth of MoS_2/WS_2 and WS_2/MoS_2 Vertical Stacks on Au Foils for Direct Photocatalytic Applications. *Adv. Mater.* **2016**, *28*, 10664–10672.

(39) Lu, Q.; Yu, Y.; Ma, Q.; Chen, B.; Zhang, H. 2D Transition-Metal-Dichalcogenide-Nanosheet-Based Composites for Photocatalytic and Electrocatalytic Hydrogen Evolution Reactions. *Adv. Mater.* **2016**, *28*, 1917–1933.

(40) Mao, J.; Wang, Y.; Zheng, Z.; Deng, D. The Rise of Two-Dimensional MoS_2 for Catalysis. *Front. Phys.* **2018**, *13*, 138118.

(41) Li, H.; Tsai, C.; Koh, A. L.; Cai, L.; Contryman, A. W.; Fragapane, A. H.; Zhao, J.; Han, H. S.; Manoharan, H. C.; Abild-Pedersen, F.; Nørskov, J. K.; Zheng, X. Activating and Optimizing MoS_2 Basal Planes for Hydrogen Evolution through the Formation of Strained Sulphur Vacancies. *Nat. Mater.* **2016**, *15*, 48–53.

(42) Peng, Z.; Chen, X.; Fan, Y.; Srolovitz, D. J.; Lei, D. Strain Engineering of 2D Semiconductors and Graphene: From Strain Fields to Band-Structure Tuning and Photonic Applications. *Light Sci. Appl.* **2020**, *9*, 190.

(43) Qi, Y.; Sadi, M. A.; Hu, D.; Zheng, M.; Wu, Z.; Jiang, Y.; Chen, Y. P. Recent Progress in Strain Engineering on Van Der Waals 2D Materials: Tunable Electrical, Electrochemical, Magnetic, and Optical Properties. *Adv. Mater.* **2023**, *35*, 2205714.

(44) Cianci, S.; Blundo, E.; Felici, M.; Polimeni, A.; Pettinari, G. Tailoring the Optical Properties of 2D Transition Metal Dichalcogenides by Strain. *Opt. Mater.* **2022**, *125*, 112087.

(45) Krasnozhon, D.; Lembke, D.; Nyffeler, C.; Leblebici, Y.; Kis, A. MoS_2 Transistors Operating at Gigahertz Frequencies. *Nano Lett.* **2014**, *14*, 5905–5911.

(46) Cheng, R.; Jiang, S.; Chen, Y.; Liu, Y.; Weiss, N.; Cheng, H.-C.; Wu, H.; Huang, Y.; Duan, X. Few-Layer Molybdenum Disulfide Transistors and Circuits for High-Speed Flexible Electronics. *Nat. Commun.* **2014**, *5*, 5143.

(47) Chang, H.-Y.; Yogeesh, M. N.; Ghosh, R.; Rai, A.; Sanne, A.; Yang, S.; Lu, N.; Banerjee, S. K.; Akinwande, D. Large-Area Monolayer MoS_2 for Flexible Low-Power RF Nanoelectronics in the GHz Regime. *Adv. Mater.* **2016**, *28*, 1818–1823.

(48) Hong, J.; Hu, Z.; Probert, M.; Li, K.; Lv, D.; Yang, X.; Gu, L.; Mao, N.; Feng, Q.; Xie, L.; Zhang, J.; Wu, D.; Zhang, Z.; Jin, C.; Ji, W.; Zhang, X.; Yuan, J.; Zhang, Z. Exploring Atomic Defects in Molybdenum Disulphide Monolayers. *Nat. Commun.* **2015**, *6*, 6293.

(49) Zhou, W.; Zou, X.; Najmaei, S.; Liu, Z.; Shi, Y.; Kong, J.; Lou, J.; Ajayan, P. M.; Yakobson, B. I.; Idrobo, J.-C. Intrinsic Structural Defects in Monolayer Molybdenum Disulfide. *Nano Lett.* **2013**, *13*, 2615–2622.

(50) Bertoldo, F.; Unocic, R. R.; Lin, Y.-C.; Sang, X.; Puretzky, A. A.; Yu, Y.; Miakota, D.; Rouleau, C. M.; Schou, J.; Thygesen, K. S.; Geohegan, D. B.; Canulescu, S. Intrinsic Defects in MoS_2 Grown by Pulsed Laser Deposition: From Monolayers to Bilayers. *ACS Nano* **2021**, *15*, 2858–2868.

(51) Gao, D.; Xia, B.; Wang, Y.; Xiao, W.; Xi, P.; Xue, D.; Ding, J. Dual-Native Vacancy Activated Basal Plane and Conductivity of MoSe2 with High-Efficiency Hydrogen Evolution Reaction. *Small* **2018**, *14*, 1704150.

(52) Lin, Z.; Carvalho, B. R.; Kahn, E.; Lv, R.; Rao, R.; Terrones, H.; Pimenta, M. A.; Terrones, M. Defect Engineering of Two-Dimensional Transition Metal Dichalcogenides. *2D Mater.* **2016**, *3*, 022002.

(53) Zhang, X.; Liao, Q.; Kang, Z.; Liu, B.; Liu, X.; Ou, Y.; Xiao, J.; Du, J.; Liu, Y.; Gao, L.; Gu, L.; Hong, M.; Yu, H.; Zhang, Z.; Duan, X.; Zhang, Y. Hidden Vacancy Benefit in Monolayer 2D Semiconductors. *Adv. Mater.* **2021**, *33*, 2007051.

(54) Woomer, A. H.; Druffel, D. L.; Sundberg, J. D.; Pawlik, J. T.; Warren, S. C. Bonding in 2D Donor–Acceptor Heterostructures. *J. Am. Chem. Soc.* **2019**, *141*, 10300–10308.

(55) Kresse, G.; Furthmüller, J. Efficiency of Ab-Initio Total Energy Calculations for Metals and Semiconductors Using a Plane-Wave Basis Set. *Comput. Mater. Sci.* **1996**, *6*, 15–50.

(56) Kresse, G.; Furthmüller, J. Efficient Iterative Schemes for Ab Initio Total-Energy Calculations Using a Plane-Wave Basis Set. *Phys. Rev. B* **1996**, *54*, 11169–11186.

(57) Kresse, G.; Joubert, D. From Ultrasoft Pseudopotentials to the Projector Augmented-Wave Method. *Phys. Rev. B* **1999**, *59*, 1758–1775.

(58) Blöchl, P. E. Projector Augmented-Wave Method. *Phys. Rev. B* **1994**, *50*, 17953–17979.

(59) Perdew, J. P.; Burke, K.; Ernzerhof, M. Generalized Gradient Approximation Made Simple. *Phys. Rev. Lett.* **1996**, *77*, 3865–3868.

(60) Klimeš J.; Bowler D. R.; and Michaelides A. Chemical Accuracy for the van Der Waals Density Functional. *J. Phys. Condens. Matter* **2010**, *22*, 022201.

(61) Klimeš, J.; Bowler, D. R.; Michaelides, A. Van Der Waals Density Functionals Applied to Solids. *Phys. Rev. B* **2011**, *83*, 195131.

(62) Silvi, B.; Savin, A. Classification of Chemical Bonds Based on Topological Analysis of Electron Localization Functions. *Nature* **1994**, *371*, 683–686.

(63) Zhao, X.-G.; Zhou, K.; Xing, B.; Zhao, R.; Luo, S.; Li, T.; Sun, Y.; Na, G.; Xie, J.; Yang, X.; Wang, X.; Wang, X.; He, X.; Lv, J.; Fu, Y.; Zhang, L. JAMIP: An Artificial-Intelligence Aided Data-Driven Infrastructure for Computational Materials Informatics. *Sci. Bull.* **2021**, *66*, 1973–1985.

(64) Nørskov, J. K.; Bligaard, T.; Logadottir, A.; Kitchin, J. R.; Chen, J. G.; Pandelov, S.; Stimming, U. Trends in the Exchange Current for Hydrogen Evolution. *J. Electrochem. Soc.* **2005**, *152*, J23–J26.

(65) Sun, Y.; Zhao, L.; Pickard, C. J.; Hemley, R. J.; Zheng, Y.; Miao, M. Chemical Interactions That Govern the Structures of Metals. *Proc. Natl. Acad. Sci.* **2023**, *120*, e2218405120.

(66) Sun, Y.; Miao, M. Chemical Templates That Assemble the Metal Superhydrides. *Chem* **2023**, *9*, 443–459.

(67) Zhang, X.; Xiao, Z.; Lei, H.; Toda, Y.; Matsuishi, S.; Kamiya, T.; Ueda, S.; Hosono, H. Two-Dimensional Transition-Metal Electride Y_2C. *Chem. Mater.* **2014**, *26*, 6638–6643.

(68) Miao, M. S.; Hoffmann, R. High-Pressure Electrides: The Chemical Nature of Interstitial Quasiatoms. *J. Am. Chem. Soc.* **2015**, *137*, 3631–3637.

(69) Krämer, K.; Schleid, T.; Schulze, M.; Urland, W.; Meyer, G. Three Bromides of Lanthanum: $LaBr_2$, La_2Br_5, and $LaBr_3$. *Z. Für Anorg. Allg. Chem.* **1989**, *575*, 61–70.

(70) Tong, W.-Y.; Gong, S.-J.; Wan, X.; Duan, C.-G. Concepts of Ferrovalley Material and Anomalous Valley Hall Effect. *Nat. Commun.* **2016**, *7*, 13612. DOI:10.1038/ncomms13612.

(71) Zhou, M.; Wang, W.; Lu, J.; Ni, Z. How Defects Influence the Photoluminescence of TMDCs. *Nano Res.* **2021**, *14*, 29–39.

(72) Zhang, X.; Gao, L.; Yu, H.; Liao, Q.; Kang, Z.; Zhang, Z.; Zhang, Y. Single-Atom Vacancy Doping in Two-Dimensional Transition Metal Dichalcogenides. *Acc. Mater. Res.* **2021**, *2*, 655–668.

(73) Liu, Y.; Wu, J.; Hackenberg, K. P.; Zhang, J.; Wang, Y. M.; Yang, Y.; Keyshar, K.; Gu, J.; Ogitsu, T.; Vajtai, R.; Lou, J.; Ajayan, P. M.; Wood, B. C.; Yakobson, B. I. Self-Optimizing, Highly Surface-Active Layered Metal Dichalcogenide Catalysts for Hydrogen Evolution. *Nat. Energy* **2017**, *2*, 1–7.

(74) Naik, M. H.; Jain, M. Substrate Screening Effects on the Quasiparticle Band Gap and Defect Charge Transition Levels in MoS_2. *Phys. Rev. Mater.* **2018**, *2*, 084002.

(75) Zhu, Q.; Chen, W.; Cheng, H.; Lu, Z.; Pan, H. WS_2 Nanosheets with Highly-Enhanced Electrochemical Activity by Facile Control of Sulfur Vacancies. *ChemCatChem* **2019**, *11*, 2667–2675.

(76) Li, L.; Qin, Z.; Ries, L.; Hong, S.; Michel, T.; Yang, J.; Salameh, C.; Bechelany, M.; Miele, P.; Kaplan, D.; Chhowalla, M.; Voiry, D. Role of Sulfur Vacancies and Undercoordinated

Mo Regions in MoS_2 Nanosheets toward the Evolution of Hydrogen. *ACS Nano* **2019**, *13*, 6824–6834.

(77) Wang, X.; Zhang, Y.; Si, H.; Zhang, Q.; Wu, J.; Gao, L.; Wei, X.; Sun, Y.; Liao, Q.; Zhang, Z.; Ammarah, K.; Gu, L.; Kang, Z.; Zhang, Y. Single-Atom Vacancy Defect to Trigger High-Efficiency Hydrogen Evolution of MoS_2. *J. Am. Chem. Soc.* **2020**, *142*, 4298–4308.

(78) Tu, Y.; Deng, J.; Ma, C.; Yu, L.; Bao, X.; Deng, D. Double-Layer Hybrid Chainmail Catalyst for High-Performance Hydrogen Evolution. *Nano Energy* **2020,** *72,* 104700.